Mechanism of metal dusting corrosion by pitting of a chromia-forming alloy at atmospheric pressure and low gas velocity

Aurélien Fabas [a], Daniel Monceau [a,*], Claudie Josse [b], Pascal Lamesle [c], Aurélie Rouaix-Vande Put [a]

[a] CIRIMAT, Université de Toulouse, CNRS, INPT, UPS, ENSIACET, 4 allée Emile Monso, BP 44362, 31030 Toulouse Cedex 4, France
[b] UMS Castaing, Université de Toulouse, ECA, 3 rue Caroline Aigle, 31400 Toulouse, France
[c] ICA (Institut Clément Ader), Université de Toulouse, Mines Albi, INSA, ISAE, UPS, Campus Jarlard, F-81013 Albi cedex 09, France

A B S T R A C T

FeNiCr samples (800HT) were exposed at 570 °C, 1 bar to a 47.25CO-47.25H_2-5.5H_2O atmosphere (a_c = 33) flowing at 18 μm/s. Pitting corrosion was observed. Pits showed a flattened morphology and a constant pit diameter growth rate. Corrosion rings appeared successively at the surface during pit growth. A four-step mechanism is proposed which includes internal oxidation of carbides, graphitisation and localised enhanced graphitisation. Gas velocity and thermal cycling play key roles in pit morphology. Thermal cycling induces circular cracks. Low gas velocity induces the gas to evolve in crevices, due to local oxygen consumption.

Keywords:
A. steel
C. high temperature corrosion
C. carburization
C. internal oxidation

1. Introduction

Metal dusting is a catastrophic form of corrosion affecting Ni-, Fe- and Co-based alloys when exposed to highly carburising atmospheres ($a_c >> 1$) [1,2]. The alloy disintegrates into a dust of fine metallic particles and graphitic carbon, named "coke". Although multiple studies were performed to determine metal dusting degradation mechanism, this complex process is still not well understood [3,4]. The combined influence of the composition of the alloy [3,5,6], of its microstructure [7,8] and of the environment [9–12] explains these difficulties. Multiple mechanisms were proposed for ferritic [2,4,13,14] and austenitic [5,15] materials. It is usually agreed that a cementite scale forms at the surface of low-alloyed ferritic materials. Hochman [1,2] and Grabke [10,16] proposed it decomposes into iron and carbon, leading to the scale and alloy degradation, while Young et al. [4] proposed the graphite nucleation at the surface and at the defects of this cementite scale leads to metal dusting. However the authors correlated the metal dusting degradation rate of low-alloyed austenitic materials to the epitaxial relationship between graphite and austenite [17–19]. Early works by Grabke and coworkers [19,20], Pippel et al. [17] and Chun et al. [18] proposed that metal dusting occurs by the inward growth of graphite whose basal planes are approximately normal to the sample surface. Several years later Zeng and Natesan [15] put forward that graphite nucleation occurred inside the metallic alloys at the most catalytic interfaces. Finally, Zhang et al. [21] proposed that metal dusting occurred by the graphite nucleation and growth along the catalytic plans intersecting the initial surface. Although there is no general agreement on the metal dusting corrosion mechanisms, they were extended to Cr_2O_3- and Al_2O_3-forming alloys but locally, at defects of the protective oxide scale [4,22,23]. However, internal oxidation could also play a key role in the degradation [24–26]. The study of the corrosion mechanisms of Cr_2O_3- or Al_2O_3-forming alloys were made either at atmospheric pressure at temperatures higher than 600 °C [5,13,14,24–26] or at high pressure at 540 °C to reproduce industrial conditions [26,27]. Unfortunately, gas flow rate is hardly specified in the studies detailing corrosion mechanisms, and its effect is not developed, despite the fact that the gas mixtures are out of equilibrium. Combining the few studies which observed the influence of gas flow rate on the kinetics of carbon deposition or metal dusting [28–30], it can anyway be concluded that gas velocity influences degradation kinetics up to a maximum flux. Indeed, when gas velocity is high enough, the frequent renewal of the gas mixture at the surface of the sample keeps the reactive gas mixture constantly equal to the input one at the reaction front. However, the possible influence of gas flow rate on corrosion mechanism was not reported, particularly at relatively low temperature. The present work tends to determine the

* Corresponding author.
E-mail address: daniel.monceau@ensiacet.fr (D. Monceau).

http://dx.doi.org/10.1016/j.corsci.2016.02.033

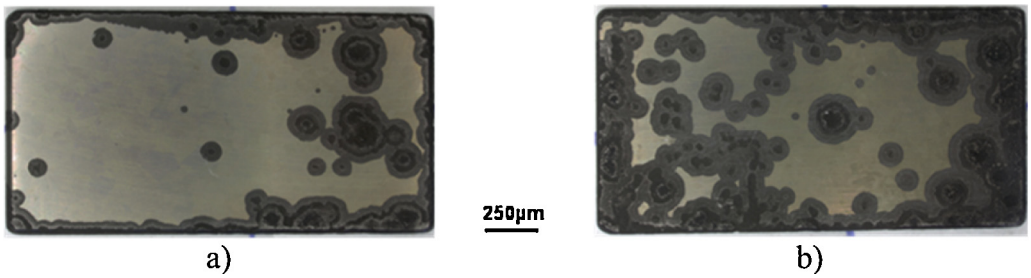

Fig. 1. Optical micrographs of (a) the external and (b) the internal face of a 800HT sample after 4000 h of exposure.

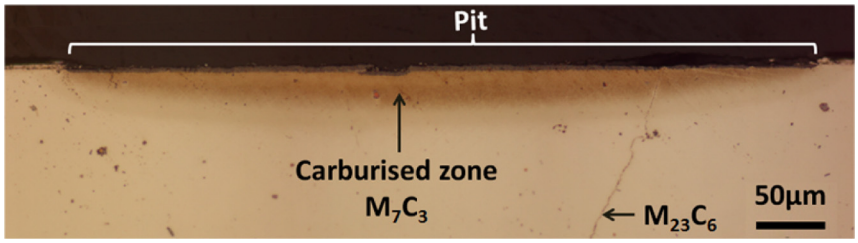

Fig. 2. Optical micrograph of the cross section of a 800HT sample after Murakami's etching and 4000 h of exposure.

pitting corrosion mechanisms occurring at atmospheric pressure below 600 °C under a low gas velocity.

2. Experimental procedure

A metal dusting experiment was carried out in a 47.25CO-47.25H_2-5.5H_2O gas mixture at 570 °C and atmospheric pressure on 800HT samples. The alloy is austenitic. Its composition is 29Ni-45Fe-21Cr-1.3Si-0.9Al-0.7Ti-0.3C-0.2Cu-0.2Mo-0.2 P for the main elements, in at.%. Water vapour pressure was established by saturating a 50CO-50H_2 mixture with water at 35 °C. The gas flow rate was about 0.2 µL/s/cm^2 of sample surface area and the gas velocity was about 18 µm/s. The experiment was conducted in a heated horizontal quartz tube. Samples rested on an alumina sample holder. Two identical samples were positioned upstream and downstream to confirm that the gas composition did not evolve during its flow. Considering only equilibrium of syngas reaction ($CO + H_2 = C + H_2O$) and water decomposition ($H_2O = H_2 + ½O_2$), a carbon activity (a_c) of 33 and an oxygen partial pressure (P_{O_2}) of 2.1×10^{-27} bar, were determined, respectively. The syngas reaction was used to determine a_c, as usual in metal dusting studies, because of its faster kinetics compared to Boudouard reaction [29]. Water decomposition was used to determine P_{O_2} instead of carbon monoxide decomposition for the same reason [31]. Sample surface was ground using P600 SiC grit paper and the edges were chamfered. The samples were removed every 500 h, cleaned ultrasonically in ethanol and weighted. Pictures of both sides of each sample were taken at every withdrawal by a Keyence VHX-1000E digital microscope. The image resolution was about 4 µm/pixel. Raman spectroscopy was carried out every two withdrawals using a Labram HR 800 Yvon Jobin spectrometer equipped with a confocal microscope (magnifications are 10×, 50× and 100×). As the different 800HT samples showed similar behaviour, one sample was removed after a total exposure of 4 000 h. Its net mass change was −4.49 mg/cm^2. Topographical mappings were carried out for several pits on an extended field confocal microscope AltiSurf520 with a 2-µm step using a chromatic sensor with a 10 nm axial resolution. The sample was also examined with a SEM/FIB FEI HELIOS 600i coupled with an EDX analyser Aztec Advanced equipped with a SDD detector. Analyses were performed using a 5 keV accelerating voltage.

3. Results and discussion

Corrosion of the samples was characterised by pitting (Fig. 1). As pitting is more pronounced at the edge of the sample, mass loss does not represent the real material degradation but rather the sample degradation with a size and shape effect. This heterogeneous pitting could be explained by an enhanced carburisation, internal oxidation and Cr-depletion at the edges due to a higher surface/volume ratio. It is also certainly due to an oxide scale containing more defects due to higher mechanical stresses at this location. The follow-up of pitting is then a more accurate way to evaluate metal dusting corrosion of materials capable to form a protective oxide scale, as performed in [32,33].

A carburised zone composed of M_7C_3 carbides was revealed below the pits by Murakami's etching on cross section (Fig. 2), according to Vander Voort [34]. Considering the alloy composition, it is assumed that this carbides are iron-chromium carbides. This carburised zone was thicker at the centre of the pits. This morphology was observed for every analysed pit. $M_{23}C_6$ carbides were identified at grain boundaries by Murakami's etching [34]. They were also assumed as iron-chromium carbides.

It was found that, at the surface of the sample, pit diameter grows at a constant rate (Fig. 3a). This kinetics can be characterised by a lateral pit growth rate constant k_d of 0.82 ± 0.02 µm/h and of 1.05 ± 0.04 µm/h on the external side (facing the quartz tube) and on the internal side (facing the centre of the quartz tube), respectively. A linear lateral pit growth kinetics has already been reported for 800HT alloy at high pressure in a previous study [33]. As all pits present a similar morphology, the following characterisation of a single pit at the centre of the internal face extends to every pit. Pit growth is characterised by the appearance of successive corrosion rings, noted CRA to CRE (for Corrosion Ring A to E), on Fig. 3b the CRA was visible after 2000 h of exposure. The CRB and the CRC, respectively at the centre and around CRA, were detected after 2500 h of exposure. Study of other pits showed that the CRB appeared when the pit diameter was about 250 µm, while the CRC appeared when the distance between the pit edge and the CRB was equal. The CRD was also visible after 2500 h of exposure and was the most external ring. After 4000 h, the CRE was detected around the CRD. A thin groove separates the CRD and the CRE. This thin groove is always at about 150 µm from the pit edge and 100 µm from the

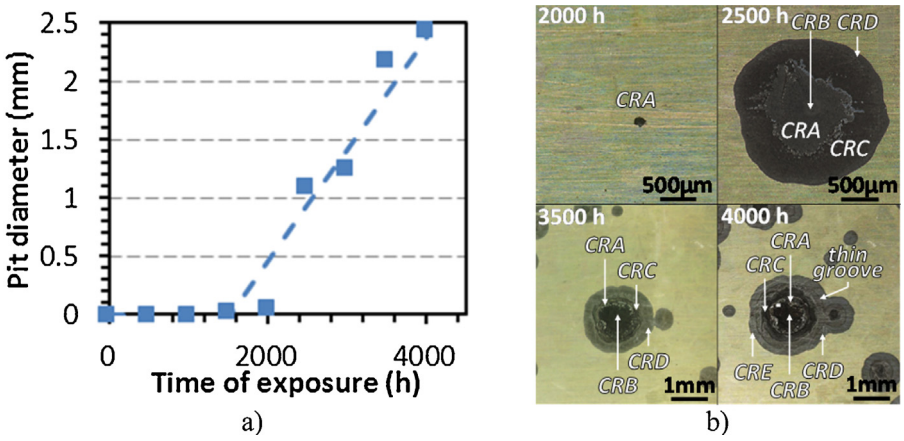

Fig. 3. (a) Evolution of the diameter of the pit at the centre of the internal face on Fig. 1 showing experimental data (squares) and linear regression (dotted line) and (b) optical images of the pit every 500 h between 2000 h and 4000 h of exposure.

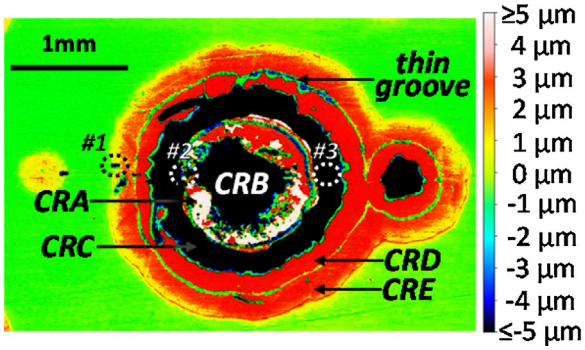

Fig. 4. Topography mapping of the pit of Fig. 3 after 4000 h of exposure. #1, #2 and #3 indicate where FIB abrasion were made.

CRC, as observed on numerous pits. Carbon and $(Fe,Cr)_3O_4$ spinel oxide were detected by Raman spectroscopy over the entire pit, except for the CRA and the CRB where only carbon was detected. The almost perfect circularity of the pits and the corrosion rings shows that their growth does not depend on the microstructure of the alloy.

The study of the pit topography (Fig. 4) revealed that the CRB and the CRC are below the initial sample surface, down to about 70 µm. The CRD and the CRE are several micrometres above the initial surface, whereas the CRA is at about 20 µm above the initial surface. The thin groove between the CRD and the CRE is a few micrometres below them. The same characteristics were observed on other pits, the number of corrosion rings depending on the time spent since incubation of the pit. The observations and assertions proposed further in this paper for a single pit are then extendable to every observed pit.

FIB analysis carried out at the edge of the pit (see #1 on Fig. 4) shows internal oxidation occurring below a Cr-depleted area (Fig. 5a). Graphitisation of the Cr-depleted alloy in the internal oxidation zone but also beneath the oxide scale is also visible. The Cr-depleted zone beneath the oxide scale has a thickness of about 1 µm and a very fine recrystallized microstructure. It is clear that internal oxidation pushes the protective chromia scale upward. This is due to the large volume increase when Cr carbides are oxidised. Indeed, the volume expansion of the alloy due to Cr_7C_3 formation is about 5% considering all the chromium reacted. The volume expansion of the alloy due to carbide oxidation into $FeCr_2O_4$ is about 48%, i.e. 41% compared to the carburised alloy. The internal oxidation thickness below the Cr-depleted alloy increases as the result of solid-state diffusion of oxygen in the metallic matrix. Thus, it follows a parabolic law [35]. In the same time, the internal oxidation thickness decreases by the material removal on top of it resulting from the volume expansion due to carbide oxidation. Carbide oxidation occurs at the internal carburisation/internal oxidation interface. On top of it, the removal of the Cr-depleted alloy and the oxide scale, consecutively to volume expansion, takes place at the internal oxidation/atmosphere interface, where the induced stress is maximised, see Fig. 5a Pit lateral growth originates from this removal and is characterised by the lateral pit growth rate constant k_d, explicated earlier. The combination of solid state diffusion and material removal leads to the following rate equation:

$$\frac{dx_{ox}}{dt} = \frac{k_{ox}}{x_{ox}} - k_d \tag{1}$$

with x_{ox} the internal oxidation thickness below the Cr-depleted zone, k_{ox} the parabolic internal oxidation constant and t the duration of exposure. This equation shows that the thickness x_{ox} increases until it reaches a constant value at the steady state, x_{ox}^{SS}, i.e. when $dx_{ox}/dt = 0$:

$$x_{ox}^{SS} = \frac{k_{ox}}{k_d} \tag{2}$$

Based on observations this thickness is comprised between 3 and 5 µm. Combining the x_{ox}^{SS} and k_d values measured in the current study, the parabolic internal oxidation constant is comprised between 2.8×10^{-12} and 1.5×10^{-11} cm^2/s. This experimental value is compared with the theoretical value calculated using the internal oxidation kinetic model [35,36] and considering chromium and iron diffusion much slower than oxygen diffusion and $FeCr_2O_4$ as the internal oxide. This lead to the following:

$$k_{ox} = \varepsilon \frac{3}{4} \frac{D_O^{eff} C_O^s}{\frac{1}{3}C_{Fe}^0 + \frac{2}{3}C_{Cr}^0} \tag{3}$$

with ε a labyrinth factor (taken equal to 1) C_{Fe}^0 and C_{Cr}^0 the bulk iron and chromium concentrations respectively, and C_O^s the oxygen concentration within the Cr-depleted alloy at the internal oxidation/atmosphere interface. C_O^s was calculated using Sievert's law and a free energy of oxygen solubilisation of −129.5 kJ/mol − obtained with a mixture law between pure Ni [37] and pure γ-Fe [38] and considering the Fe/Ni ratio of the 800HT alloy. The effective oxygen diffusion coefficient, D_O^{eff}, was determined using Hart's formula [39]:

$$D_O^{eff} = \left(1 - \frac{q}{L}\delta\right) D_O^b + \frac{q}{L}\delta D_O^{gb} \tag{4}$$

where q is the shape factor of grains, considered as cubic (i.e. a q value of 3), L is the grain size of the alloy (which is about 500 µm), δ

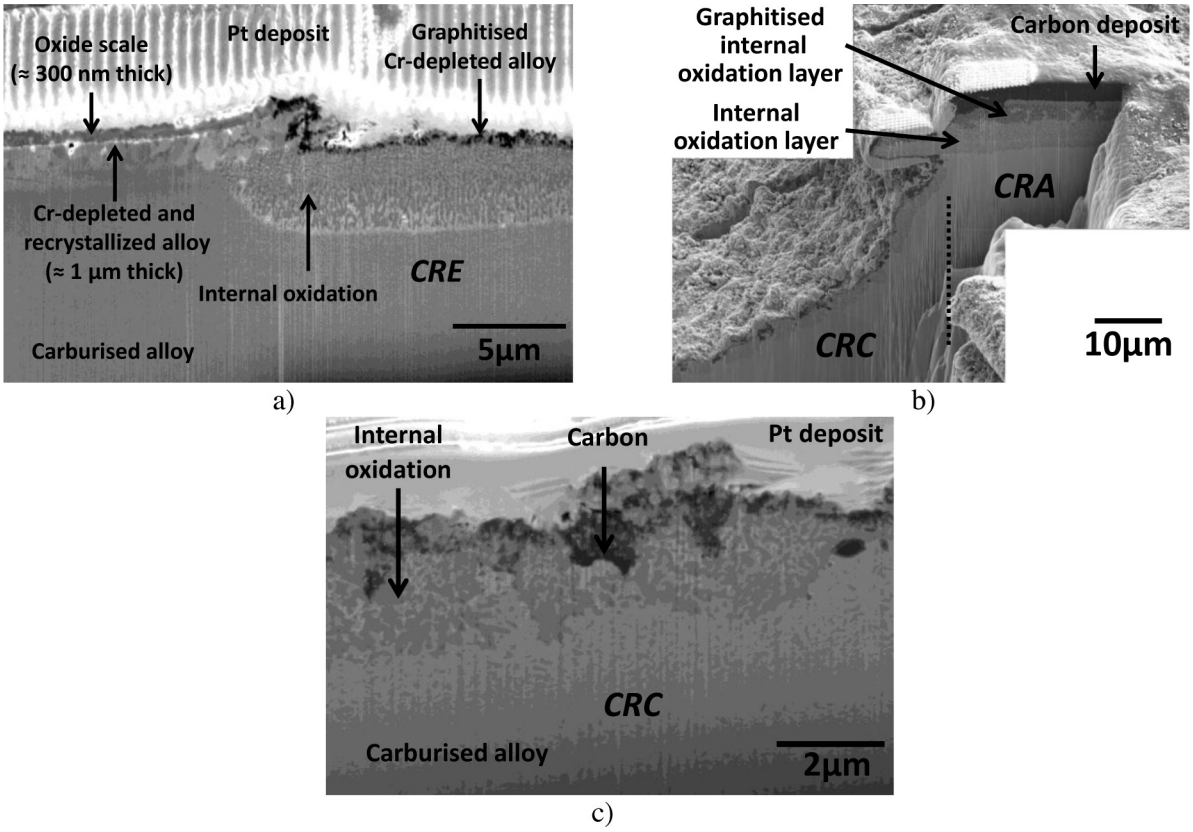

Fig. 5. SEM micrograph in BSE mode of FIB cross sections (a) #1 at the edge (CRE), (b) #2 between CRA and CRC and (c) #3 at the bottom of CRC of the pit on Fig. 3 after 4000 h of exposure.

is the width of grain boundaries (taken equal to 1 nm), D_O^b is the oxygen diffusion coefficient in the bulk. Its value of 1.2×10^{-10} cm^2/s was determined by a linear mixture law between the oxygen diffusion coefficients in pure Ni [37] and pure γ-Fe [38] with the Fe/Ni ratio corresponding to the one of 800HT alloy. D_O^{gb} was estimated considering it was about 5 orders of magnitude higher than D_O^b.The obtained value of D_O^{eff}, equal to 2.0×10^{-10} cm^2/s, is about two times higher than D_O^b. Based on Eq. (3), a value of $k_{ox} = 2.3 \times 10^{-11}$ cm^2/s is obtained. This value is higher but in reasonable agreement with the experimental one -2.8×10^{-12} to 1.5×10^{-11} cm^2/s, considering the finer microstructure beneath the oxide scale is not taken into account in calculation, in addition with the lack of data at this low temperature, particularly for diffusion at grain boundaries. The use of a linear mixture law to determine C_O^s and D_O^{eff} at this low temperature is also a source of error. Moreover graphitisation occurs in the same time as oxidation, increasing pit lateral growth (Fig. 5a). Finally, the theory used to calculate the parabolic constant k_{ox} considers precipitation of internal oxide and not oxidation of internal carbides. The agreement between calculated and experimental parabolic oxidation constants allows to conclude that pit lateral growth kinetics is consistent with a control by the kinetics of internal oxidation of carbides below the Cr-depleted zone. The detection of $(Fe,Cr)_3O_4$ as internal oxide instead of the more stable Cr_2O_3 can be explained by the oxidation of the $(Fe,Cr)_7C_3$ carbides in a Cr-depleted matrix. The released carbon is expected to diffuse inward to form new carbides, as observed by Meijering et al. [40] and other studies (see Ref. [31]).

One can notice that the calculated parabolic constant of the internal oxidation kinetics is close to the ones generally observed under an oxide scale. Indeed, the oxygen partial pressures usually observed in metal dusting environments are close to the ones corresponding to the metal/oxide equilibrium. For instance, the oxygen partial pressure of the input gas mixture is $P_{O_2} = 2.1 \times 10^{-27}$ bar which is only one order of magnitude lower than the oxygen partial pressure of the Fe/FeO equilibrium determined via an Ellingham magnitude lower than the oxygen partial pressure of the Fe/FeO equilibrium determined via an Ellingham diagram: $P_{O_2}^{Fe/FeO} \approx 10^{-26}$ bar. The internal oxidation kinetics in this study is then equivalent to the one under a FeO oxide scale, considering the Ni/Fe ratio of the 800HT for the matrix.

FIB analysis carried out at the interface between the CRA and the CRC (Fig. 5b, #2 on Fig. 4) shows a 8 µm-thick continuous internal oxidation layer in the CRA. Although the inner zone of this layer is composed of spinel and Cr-depleted alloy, the outer zone is composed of spinel and carbon. It is concluded that the Cr-depleted alloy is graphitised by the highly carburising atmosphere. A thick carbon deposit is visible on top of the alloy. This adherent carbon explains why the CRA is higher than the other corrosion rings, as observed on Fig. 4. It is also consistent with the carbon signal obtained by Raman spectroscopy.

At the bottom of the CRC (Fig. 5c, and #3 on Fig. 4) and on the sloping corrosion front visible on Fig. 5b, it can be seen that the thickness of the internal oxidation layer is thinner than described previously for other corrosion rings. It is also discontinuous. Locally, carbon deposit is in direct contact with the carburised alloy. This morphology is very different from what is observed for the CRA and the CRB. Such difference, associated with a faster inward growth of the corrosion ring, shows that the degradation mechanism in the CRC differs. This localised degradation, occurring only in this "deep" ring, could be explained by the lack of atmosphere renewal in this area. Oxygen consumption by internal oxidation coupled with the lack of gas renewal leads to a reduced oxygen concentration in the gas phase and at the metal surface. This could explain why the internal oxidation layer is thinner than at the planar surface of the pit

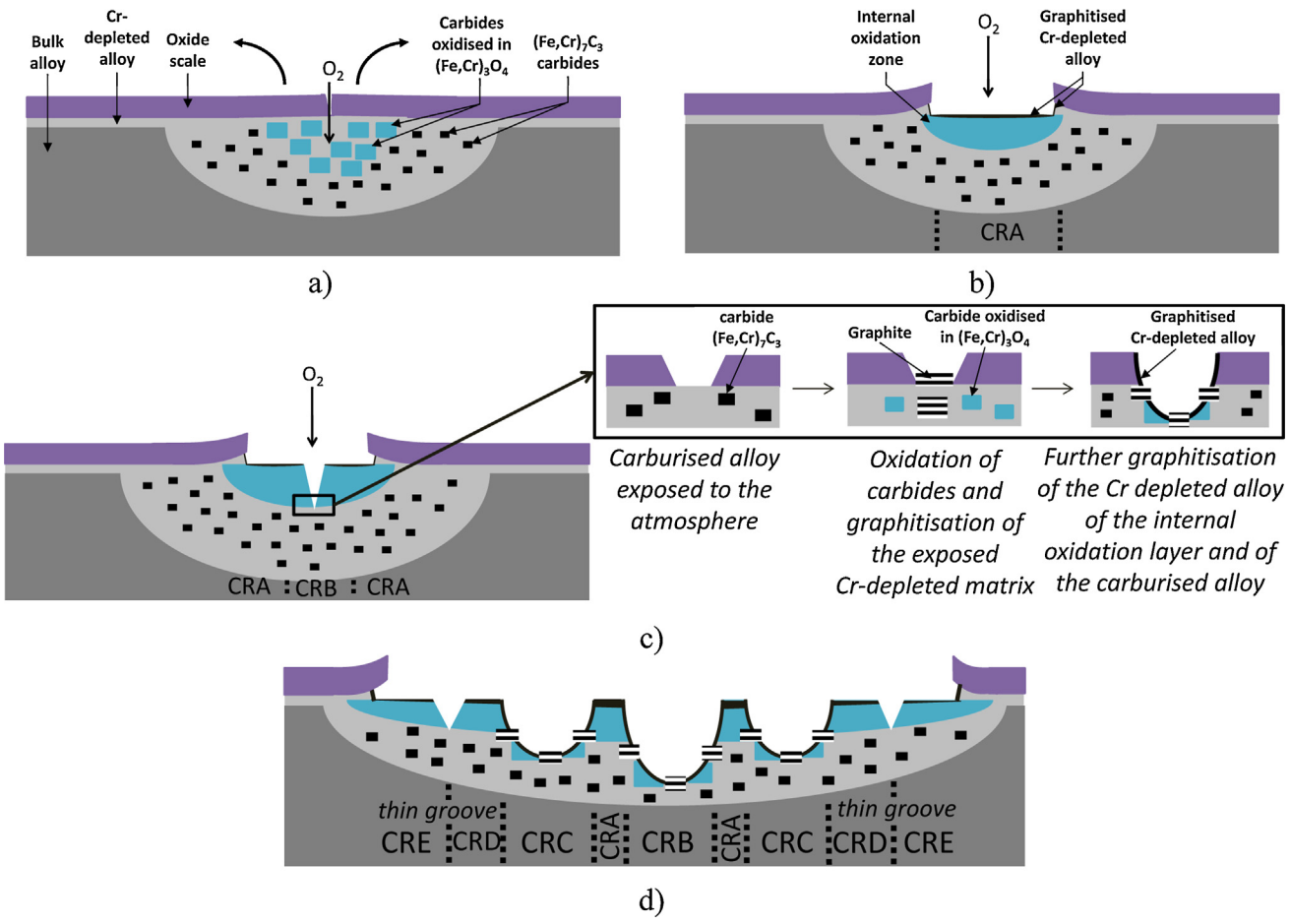

Fig. 6. Scheme of the proposed four-step mechanism: (a) oxidation of carbides, the arrows represent the outward push of the oxide scale due to internal oxidation; (b) graphitisation of the Cr-depleted alloy; (c) enhanced graphitisation at the bottom of the thermal crack (the mechanism is detailed in the inset); (d) lateral growth by internal oxidation and inward growth by enhanced graphitisation at the bottom of the cracks, leading to new deep corrosion rings. Corrosion rings A–E are recalled for easy comparison with Fig. 3.

and why it is discontinuous. In addition, the lack of oxygen does not allow the formation of a inhomogeneous internal oxidation layer. This results in a direct exposure to the carburising atmosphere of the Cr-depleted alloy of the internal oxidation and of the carburised alloy. The Cr-depleted alloy is then graphitised in agreement with the Fe-Cr-C phase equilibrium. Moreover, the local oxygen consumption leads to a higher surface fraction of alloy available for CO and H_2 adsorption, enhancing the graphitisation.

The FIB study of the thin groove between the CRD and the CRE shows a morphology similar to the one observed at the bottom of the CRC. As noticed previously, this thin groove is always at about 150 μm from the edge of the pit, and at about 100 μm from the CRC. As already explained, the almost perfect circularity of the groove and its size larger than the one of the alloy grains reveal the groove shape is not controlled by the alloy microstructure. One could think that this groove finds its origin in the thermal cycling every 500 h. To confirm or invalidate this, the mechanical properties and the evolution of the coefficients of thermal expansion (CTE) with temperature of 800HT alloy [41] and of $(Fe,Cr)_3O_4$ [42] have to be considered. At the beginning of the cooling, the CTE of the internal oxidation zone – determined using a mixture law between the CTEs of 800HT and $(Fe,Cr)_3O_4$–is initially higher than the CTE of the 800HT alloy. This can be surprising, but it is due to the fact that the CTE of the spinel is higher than the one of the metallic alloy at 570 °C. Sample cooling then generates tensile stress in the internal oxidation zone. This tensile stress is expected to reach its highest value at a temperature around 370 °C, when the CTEs of 800HT and of the internal oxidation zone become equal. This leads to the localised rupture where the stress is maximised. The tensile stress necessary to initiate the crack within the internal oxidation layer happens when the width of the CRD – i.e. the distance between the edges of the pit and the CRC – is long enough. For a CRD width of 250 μm, the stress is maximised at about 150 μm from the edge of the pit. It splits the CRD in two new corrosion rings: an inner ring (the CRD) and an outer ring (the CRE) —see Fig. 3b after 3500 h. Below 370 °C, the CTE of 800HT is higher than the CTE of the internal oxidation zone. The stress then diminishes during the residual cooling. The crack closes and results in the thin groove observed at room temperature. At the end of the cooling, there is almost no residual stress. When reheated, the defect opens and exposes the carburised alloy beneath the internal oxide layer directly to the atmosphere. Consequently, the enhanced graphitisation phenomenon develops in this groove, creating a new deep corrosion ring. This was confirmed for pits experiencing further exposure.

The proposed explanation is valid only when there is a perfect adhesion between the oxide and the matrix. Yet, as internal oxidation leads to compressive stresses, which could be much higher than the tensile stress obtained by sample cooling, and CTE mismatch, further study is necessary. Nevertheless, it is reasonable to think that the compressive stresses due to internal oxidation can be relaxed by creep during the long dwells at high temperature, leading to the thickening of the internal oxidation zone perpendicularly to the surface, whereas tensile stress due to CTE mismatch have no time to relax during cooling.

As noticed previously, the formation of the deep CRB at the centre of the CRA on Fig. 3b is supposed to happen when the pit – i.e. the CRA at this time – reaches a diameter of about 250 μm. The mechanism given previously for the thin groove could also apply at the centre of the pit, i.e. the CRA. The CRC is also expected to originate from the same phenomenon occurring to the CRA once it reaches again a width of about 250 μm. The enhanced graphitisation mechanism explains the depth of the CRB and the CRC. The CRB, the CRC and the thin groove are then three states of the same degradation phenomenon.

4. Pitting corrosion mechanism

An overall corrosion mechanism in four main steps can now be proposed to explain our observations of the pit corrosion features. First, carbon diffuses through the chromia scale despite the protective properties of this oxide. Indeed, Wolf and Grabke [43] proposed carbon diffused through protective oxide scales in pores and cracks. Zeng and Natesan [44] proposed that diffusion paths for carbon were micro-channels of metallic or cementite particles within the oxide, while Röhnert et al. [23] proposed carbon could diffuse through graphite encapsulated in the oxide scale. More recently, Young et al. [45] showed carbon diffusing through a Cr_2O_3 scale using atom probe microscopy. After its diffusion through the oxide scale, carbon continues its way in the metal and carburises the alloy beneath the Cr-depleted zone – stemmed from the formation of the protective oxide layer –, forming $(Cr,Fe)_7C_3$ carbides. As suggested by Röhnert et al. [23], the volume expansion of the alloy due to carburisation (+5%) could also induce cracks in the oxide scale, allowing the direct access of the atmosphere to the metallic surface.

Secondly, oxygen diffuses in the alloy through the defects in the oxide scale and oxidises internal $(Cr, Fe)_7C_3$ carbides into $FeCr_2O_4$ spinel oxide (Fig. 6a). This step is expected to happen when chromium concentration in the matrix is lowered due to chromium trapping by carburisation. Once the concentration is too low to support external oxidation, internal oxidation of carbides takes place [46]. The resulting local volume expansion of the internal oxidation zone (+41%) disintegrates the oxide scale and the Cr-depleted alloy. This step can be considered as the nucleation of the pit. This removal of material exposes the internal oxidation zone, and the Cr-depleted zone beneath the protective oxide scale, at the edge of the pit initiation to the external atmosphere. The lateral growth of the internal oxidation zone below the protective oxide induces pit lateral growth, pushing upward the external oxide scale. This phenomenon is accentuated by the graphitisation of the Cr-depleted alloy beneath the oxide scale because it causes an additional volume expansion. It also reduces the thickness of the Cr-depleted alloy into which the oxygen has to diffuse to react with non-oxidised carbides.

Thirdly, the Cr-depleted alloy in the internal oxidation zone is also graphitised (Fig. 6b). Moreover, a crack forms through the internal oxidation zone due to tensile stress during sample cooling, only if the pit width is greater than a critical size. When reheated, the crack opens, exposing the carburised zone beneath it. The Cr-depleted alloy is then directly exposed to the atmosphere. At the surface of the newly exposed Cr-depleted alloy, the atmosphere is not renewed, due to a microclimate in the crevice. The lack of gas renewal results in a lower oxygen partial pressure, hence a lower inward oxygen flux. This generates a thin and inhomogeneous internal oxidation layer exposing the Cr-depleted alloy of the internal oxidation zone and of the carburised alloy, to the local atmosphere. In the same time, oxygen consumption increases partial pressures of CO and H_2. The addition of the two phenomena leads to an enhanced graphitisation, hence a faster local inward degradation. This leads to the formation of a central deep corrosion disk at the centre of the pit (Fig. 6c), corresponding to the appearance of the CRB at the centre of the CRA (Fig. 4).

Finally, if the diameter of the external ring is greater than the critical value during a following cooling, a new crack will occur during cooling at the temperature when the stress is maximised. When reheated, the crack opens and the same enhanced graphitisation mechanism occurs at the bottom of the crack, as explained for the formation of the central deep corrosion disk. This forms a deep corrosion ring (Fig. 6c). This corresponds to the CRC on the studied pit, the CRA being split in an internal (CRA on Fig. 4) and an external corrosion ring, at the edge of the pit (CRD on Fig. 4). The enhanced graphitisation mechanism following crack formation leads to the formation of new deep corrosion rings during the cooling if the external corrosion ring has reached a critical width, as observed on older pits. It has to be noticed that the 250 μm width measured in this study is not this critical size but corresponds to the pit growth after 500 h of exposure. The beginning of a third deep corrosion ring is the thin groove between the CRD and the CRE (the latter being the external part of the cracked CRD) (Fig. 4). The final pit morphology after 4000 h is schematised on Fig. 6d, based on Fig. 4. For the oldest pits, i.e. for the longest durations of exposure, the deep corrosion rings merge to form a massive central deep corrosion disk.

The proposed mechanism can be viewed either as an entirely novel mechanism specific to our experimental conditions, or as the elementary reaction steps of the overall observed degradation mechanisms involving internal oxidation, with much higher gas flow rate [25,27]. Il has also to be noticed that a similar morphology can be observed in previous works, although this has not been mentioned nor studied in the considered papers [30,47,48]. The number of rings that can be observed in these articles are different than in the current study. The number of rings in this literature data cannot be quantitatively compared with our modelling since pit incubation time and pit lateral growth are not given.

5. Conclusion

A pitting mechanism is described for samples of 800HT tested under metal dusting conditions at 1 bar in CO-H_2-H_2O mixture, and withdrawn every 500 h for characterisation. The pitting mechanism is based on internal carbide oxidation and localised enhanced graphitisation of the Cr-depleted alloy. It can be divided in 4 steps:

1) Pit nucleation and growth due to the breakdown of the oxide scale induced by the large volume expansion resulting from the oxidation of previously formed carbides. The localisation of the attack is due to the presence of defects in the protective oxide scale.
2) Graphitisation of the Cr-depleted matrix of the internal oxidation zone and the one that stemmed from the external oxide scale formation.
3) Enhanced graphitisation due to a microclimate atmosphere with lower oxygen and higher carbon activities at the bottom of a crack induced by tensile stress in the internal oxidation zone during cooling.
4) Pit lateral growth controlled by the kinetics of oxidation of the carbides whereas the pit inward growth is controlled by the enhanced graphitisation at the bottom of the crack (whose merging results in an inner deep corrosion disk).

As it is explained in the proposed mechanism, the morphology of the pits is modified by thermal cycling. Indeed, the crack from which inward growth occurs is formed during sample cooling carried out for sample characterisation. This highlights the importance of the experimental procedure.

Acknowledgements

This work has been supported by the French national research agency through the project ANR SCAPAC 11-RNMP-0016 in partnership between Air Liquide, Veolia, Sedis, University of Nancy, CIRIMAT laboratory. The authors acknowledge Sabine Leroux of the ICA laboratory for daily monitoring of the experiment.

References

[1] R.F. Hochman, Metal deterioration in carbon monoxide and hydrocarbons at elevated temperatures, in: Third International Congress on Metallic Corrosion, USSR, Mir, Mosow, 1966.
[2] R.F. Hochman, Catastrophic deterioration of high-temperature alloys in carbonaceous atmospheres, in: Symposium on Properties of High Temperature Alloys with Emphasis on Environmental Effects, Las Vegas, Nevada, 1976, pp. 715–732.
[3] H.J. Grabke, Metal dusting, Mater. Corros. 54 (2003) 746.
[4] D.J. Young, J. Zhang, C. Geers, M. Schütze, Recent advances in understanding metal dusting: a review, Mater. Corros. 62 (2011) 7–28.
[5] H.J. Grabke, R. Krajak, E.M. Müller-Lorenz, S. StrauB, Metal dusting of nickel-base alloys, Mater. Corros. 47 (1996) 495–504.
[6] S. Strauß, H.J. Grabke, Role of alloying elements in steels on metal dusting, Mater. Corros. 49 (1998) 321–327.
[7] H.J. Grabke, E.M. Müller-Lorenz, B. Eltester, M. Lucas, D. Monceau, Resistance of 9–20% Cr-steels against metal dusting, Steel Res. 68 (1997) 179–185.
[8] H.J. Grabke, E.M. Müller-Lorenz, S. Strauss, E. Pippel, J. Woltersdorf, Effects of grain size, cold working, and surface finish on the metal-dusting resistance of steels, Oxid. Met. 50 (1998) 241–254.
[9] R.A. Perkins, W.C. Coons, F.J. Radd, Metal-Dusting corrosion in coal-Gasification environments, J. Electrochem. Soc. 123 (1976) 733–749.
[10] H.J. Grabke, C.B. Bracho-Troconis, E.M. Müller-Lorenz, Metal dusting of low alloy steels, Mater. Corros. 45 (1994) 215–221.
[11] A. Schneider, H. Viefhaus, G. Inden, H.J. Grabke, E.M. Müller-Lorenz, Influence of H2S on metal dusting, Mater. Corros. 49 (1998) 339.
[12] E.M. Müller-Lorenz, H.J. Grabke, Coking by metal dusting of steels, Mater. Corros. 50 (1999) 621.
[13] P. Szakálos, Mechanisms and driving forces of metal dusting, Mater. Corros. 54 (2003) 762.
[14] H.J. Grabke, R. Krajak, J.C. Nava Paz, Metal dusting of high-temperature alloys, Mater. Corros. 44 (1993) 89–97.
[15] Z. Zeng, K. Natesan, Relationship of carbon crystallization to the metal-dusting mechanism of nickel, Chem. Mat. 15 (2003) 872–878.
[16] H.J. Grabke, R. Krajak, J.C.N. Paz, On the mechanism of catastrophic carburization—metal dusting, Corros. Sci. 35 (1993) 1141–1150.
[17] E. Pippel, J. Woltersdorf, R. Schneider, Micromechanisms of metal dusting on Fe-base and Ni-base alloys, Mater. Corros. 49 (1998) 309–316.
[18] C.M. Chun, J.D. Mumford, T.A. Ramanarayanan, Carbon-induced corrosion of nickel anode, J. Electrochem. Soc. 147 (2000) 3680–3686.
[19] Q. Wei, E. Pippel, J. Woltersdorf, S. Strauss, H.J. Grabke, Orientation dependence of metal dusting nanoprocesses on nickel single crystals, Mater. Corros. Werkstoffe Korros. 51 (2000) 652–656.
[20] R. Schneider, E. Pippel, J. Woltersdorf, S. Strauss, H.J. Grabke, Microprocesses of metal dusting on nickel and Ni-base alloys, Steel Res. 68 (1997) 326–332.
[21] J.Q. Zhang, P. Munroe, D.J. Young, Microprocesses in nickel accompanying metal dusting, Acta Mater. 56 (2008) 68–77.
[22] H.J. Grabke, Thermodynamics, mechanisms and kinetics of metal dusting, Mater. Corros. 49 (1998) 303–308.
[23] D. Röhnert, F. Phillipp, H. Reuther, T. Weber, E. Wessel, M. Schütze, Initial stages in the metal-dusting process on alloy 800, Oxid. Met. 68 (2007) 271–293.
[24] P. Szakálos, R. Pettersson, S. Hertzman, An active corrosion mechanism for metal dusting on 304L stainless steel, Corros. Sci. 44 (2002) 2270.
[25] M. Hansel, C.A. Boddington, D.J. Young, Internal oxidation and carburisation of heat-resistant alloys, Corros. Sci. 45 (2003) 967–981.
[26] P. Szakálos, M. Lundberg, R. Pettersson, Metal dusting on an alumina forming Ni-base alloy, Corros. Sci. 48 (2006) 1695.
[27] J.Z. Albertsen, Ã. Grong, J.C. Walmsley, R.H. Mathiesen, W. Beek, A model for high-Temperature pitting corrosion in nickel-Based alloys involving internal precipitation of carbides, oxides, and graphite, Metall. Mater. Trans. A 39 (2008) 1258–1276.
[28] P.L. Walker, J.F. Rakszawski, G.R. Imperial, Carbon formation from carbon monoxide-hydrogen mixtures over iron catalysts. II —rates of carbon formation, J. Phys. Chem. 63 (1959) 140–149.
[29] E.T. Turkdogan, J.V. Vinters, Catalytic effect of iron on decomposition of carbon monoxide: i. carbon deposition in H2-CO mixtures, Metall. Trans. 5 (1974) 11–19.
[30] J.C. Nava-Paz, H.J. Grabke, Metal Dusting, Oxid. Met. 39 (1993) 437–456.
[31] D.J. Young, High Temperature Oxidation and Corrosion of Metals, Elsevier, Amsterdam, 2008.
[32] S.K. Varma, A. Putrevu, M. Pasala, Z. Zeng, K. Natesan, Metal dusting and oxidation at 593 and 704 °C, THERMEC 2006 (2007) 4226–4231, Pts 1–5.
[33] A. Fabas, D. Monceau, S. Doublet, A. Rouaix-Vande Put, Modelling of the kinetics of pitting corrosion by metal dusting, Corros. Sci. 98 (2015) 592–604.
[34] G. Vander Voort, E. Manilova, J.R. Michael, A study of selective etching of carbides in steel, Microsc. Microanal. 10 (2004) 76–77.
[35] R.A. Rapp, Kinetics microstructures and mechanism of internal oxidation—its effect and prevention in high temperature oxidation, corrosion, NACE 21 (1965) 382–401.
[36] C. Wagner, Reaktionstypen bei der oxydation von legierungen, Zeitschrift Elektrochem. 63 (1959) 772–790.
[37] J.-W. Park, C.J. Altstetter, The diffusion and solubility of oxygen in solid nickel, Metall. Trans. A 18A (1987) 43–50.
[38] J. Swisher, E.T. Turdogan, Solubility, permeability, and diffusivity of oxygen in solid iron, Trans. Metall. Soc. AIME 239 (1967) 426–431.
[39] E.W. Hart, On the role of dislocations in bulk diffusion, Acta Met. 5 (1957), 597–597.
[40] J.L. Meijering, Internal oxidation in alloys, in: H. Herman (Ed.), Advances in Materials Research, 5th ed., Wiley-Interscience, New York, 1971.
[41] INCOLOY® alloy 800H & 800HT® in, Special Metals Corporation Alloy specifications, (2004).
[42] J. Robertson, M.I. Manning, Criteria for the formation of single, duplex and breakaway scales on steels, Mat. Sci. Technol. 4 (1988) 1064–1071.
[43] I. Wolf, H.J. Grabke, A study on the solubility and distribution of carbon in oxides, Solid State Commun. 54 (1985) 5–10.
[44] Z. Zeng, K. Natesan, Initiation of metal-dusting pits and a method to mitigate metal-dusting corrosion, Oxid. Met. 66 (2006) 1–20.
[45] D.J. Young, T.D. Nguyen, P. Felfer, J. Zhang, J.M. Cairney, Penetration of protective chromia scales by carbon, Scr. Mater. 77 (2014) 29–32.
[46] C.S. Giggins, F.S. Pettit, Corrosion of metals and alloys in mixed gas environments at elevated-temperatures, Oxid. Met. 14 (1980) 363–413.
[47] Y. Nishiyama, N. Otsuka, T. Kudo, Metal dusting behaviour of Cr-Ni steels and Ni-base alloys in a simulated syngas mixture, Corros. Sci. 48 (2006) 2064–2083.
[48] C. Rosado, M. Schütze, Protective behaviour of newly developed coatings against metal dusting, Mater. Corros. 54 (2003) 831–853.